Optical Engineering

Optical Engineering. SPIED igital Library.org

Weather-limited in-band full-duplex transceiver model for free-space optical communication

Abul F. M. S. Haq Murat Yuksel



Abul F. M. S. Haq, Murat Yuksel, "Weather-limited in-band full-duplex transceiver model for free-space optical communication," *Opt. Eng.* **59**(5), 056113 (2020), doi: 10.1117/1.0E.59.5.056113

Weather-limited in-band full-duplex transceiver model for free-space optical communication

Abul F. M. S. Haq^{a,*} and Murat Yuksel^{a,b}

^aUniversity of Central Florida, CREOL, The College of Optics and Photonics,
 Orlando, Florida, United States
 ^bUniversity of Central Florida, Department of Electrical and Computer Engineering,
 Orlando, Florida, United States

Abstract. Free-space optical (FSO) communication has gained popularity for wireless applications over legacy radio frequency for advantages such as unlicensed operation, spatial reuse, and security. Even though FSO communication can achieve high bit rates, range limitation due to strong attenuation and weather dependency has always restricted its practical applications to controlled settings such as building-to-building communication. Futuristic mobile and secure *ad hoc* FSO network applications such as smart cars and air-subsea links need more efficient and autonomous link acquisition capabilities, which can be enabled by in-band full-duplex (IBFD) operation. We proposed an IBFD-FSO transceiver prototype consisting of off-the-shelf components to demonstrate the concept of IBFD operation by the isolation technique. We also developed a laser-based IBFD-FSO link model by incorporating an atmospheric attenuation model and self-interference cancellation model. We found that, for clear weather, the maximum achievable link range using commercially available components can be up to 120 m. We also determined weather-dependent performance of the FSO link in terms of visibility and transmit power. © 2020 Society of Photo-Optical Instrumentation Engineers (SPIE) [DOI: 10.1117/1.OE.59.5.056113]

Keywords: in-band; full-duplex; short-range; free-space optical; optical wireless.

Paper 20200274 received Mar. 5, 2020; accepted for publication May 15, 2020; published online May 28, 2020.

1 Introduction

Free-space-optical communications (FSOC) is envisioned to play a significant role in future generation wireless *ad hoc* networks. In recent years, the application of FSO transceivers has attracted strong interest from both the wireless research community and industry. ¹⁻³ FSOC uses the unlicensed optical spectrum and relies mostly on basic optoelectronic technology used in fiber-optic communications. It provides very high point-to-point data transfer rates of up to 10 Gbps⁴ and much higher bandwidth compared with traditional radio frequency (RF) networks. Moreover, FSO transceivers are highly directional and thus provide better spatial reuse and larger network capacity. This directionality also reduces the interference caused from unwanted directions and enhances signal security by lowering the probability of interception and detection by sniffers. FSO networking can be useful for multinode short-distance communication networks, which require high bandwidth and mobility. Tactical *ad hoc* networks with the requirements of high bandwidth and reduced probability of jamming and interception can greatly benefit from implementing nodes with FSO transceivers. Beyond these advantages, the network capacity can be significantly increased by utilizing the FSO transceivers, particularly with in-band full-duplex (IBFD) communications capability.

Currently, in almost all optical communication networks, the antennas/transceivers operate in half-duplex mode, where a node can either transmit or receive but cannot do both over the same communication channel at the same time. Although this results in inefficient use of resources, it helps to avoid self-interference (SI) that occurs when the mode of operation is full-duplex. IBFD communication uses simultaneous signal transmission and reception in the same frequency

0091-3286/2020/\$28.00 © 2020 SPIE

Optical Engineering 056113-1 May 2020 • Vol. 59(5)

^{*}Address all correspondence to Abul F. M. S. Haq, E-mail: saniul.haq@knights.ucf.edu

band. Despite the disadvantages caused by SI, full-duplex operation can aid in successfully dealing with large spectrum demands. Even in the presence of SI, full-duplex communication can provide at least 20% gain over half-duplex communication. ^{5,6} A multiaccess control protocol for full-duplex radio communication that helps achieve 88% throughput gain was proposed by Goyal et al. ⁷ Also the effect of SI reduces significantly with increases in directionality of the transmitter and the receiver of a node. ⁸ Recently, several other works have focused on designing directional RF transceivers, showing the feasibility of having full-duplex communication. ^{9,10}

Full-duplex communication can be achieved through active or passive SI suppression for RF transceivers. In active interference suppression, a node cancels out its own transmitted signal received by its receiver by injecting a cancellation waveform in the direction of its own receiver antenna. In passive suppression, transmitter and receiver antennas are separated by an electromagnetic observer that enforces the signal strength at the receiver coming from its own transmitter to be below the receiver's cutoff. ¹⁰ The idea of isolating the transmitter and receiver of a node using nonreflective and nontransparent material for achieving IBFD functionality has been proposed in the literature. ^{1,11} For FSO transceivers, full duplex communication can also be achieved using transmitters and receivers of separate wavelengths. ^{12–14}

In this paper, the main contributions are as follows.

- We present a prototype of a functional IBFD transceiver using off-the-shelf components to demonstrate the concept of IBFD operation by the isolation technique.¹⁵
- We model an IBFD-FSO transceiver having a bandwidth of 175 MHz using vertical-cavity surface-emitting lasers (VCSEL) as the transmitter and Si PIN photodiode as the receiver at 900 nm wavelength to determine the range and signal quality of the communication link. We incorporate atmospheric attenuation, surface reflection, and back-scattering to observe the weather dependency on the link performance. We consider the FSO beam propagation model and transmitter geometry for modeling as well as vary the transmitter power and visibility range (100 m to 25 km). We find that for clear weather (e.g., visibility being 25 km) and 10-mW transmitter power, the IBFD-FSO communication link can range up to 120 m.¹⁶
- We calculate the quality of the link in terms of signal-to-interference-plus-noise ratio (SINR) in which visibility and transmitter power are taken into account.
- We propose an analytical model for SI cancellation (SIC) due to the presence of an isolator within a transceiver unit.

The remainder of this paper is organized as follows. We discuss the motivation and literature review for IBFD operation of FSOC under different weather conditions in Sec. 2. In Sec. 3, we demonstrate an IBFD-FSO transceiver prototype by implementing an isolation mechanism within a transceiver unit. We develop a mathematical model for the communication link in Sec. 4. We incorporate the effects of atmospheric attenuation, weather conditions, and transmit power to evaluate the performance of the IBFD-FSO transceiver. Finally, link performance simulation results are presented and discussed in Sec. 5.

2 Background and Motivation

In this section, we first present the existing literature on full-duplex RF communications. Then we discuss some previous work that has addressed the problem of full-duplex transceiver design for FSO communications. We also include the weather-dependent performance studies and proposed models and how we can incorporate those models into the design and performance estimation of IBFD optical wireless communication.

2.1 Full-Duplex RF

The concept of designing full-duplex transceivers has been around since the 1940s, but recent requirements for higher bandwidth transmission ignited much interest in implementation of IBFD wireless communication systems. ^{17–19} By utilizing the IBFD mode, the ergodic capacity can theoretically be doubled compared with the half-duplex mode. ²⁰ Despite other advantages,

such as reduced end-to-end delay and improved efficiency of *ad hoc* network protocols, IBFD design has a few challenges as well, such as SI, increased internode interference, and design complexity. SIC techniques for IBFD mode operation can be classified into active and passive schemes. For active SIC, analog cancellation is done to suppress SI before it enters the analog-to-digital converter at the receiver. Active cancellation can be achieved in two ways: first, by injecting a replica transmit waveform into the receiver of the same transceiver using a Balun transformer and second, by introducing path loss and delay in the digital domain, which cancels the SI when converted into analog and added with the transmit signal. For passive SIC, SI is suppressed even before entering the receiver path in the transceiver package. This essentially means establishing an electromagnetic obstruction in the path of SI using a directional antenna or an absorbing material.

2.2 Full-Duplex FSO

The prior work on full-duplex FSOC has reported transceiver designs using out-of-band techniques. Full-duplex indoor optical wireless communication is demonstrated for error-free [i.e., bit error rate (BER) $<10^{-9}$] short-range operation. ^{12,13} The transceiver used different optical wavelengths for uplink (1550.12 nm) and downlink (850 nm) channels, which makes it an out-of-band design. To suppress the SI for full-duplex operation, two separate bands are used for the transmitter and the receiver. Wang et al.²³ reported a full-duplex visible light communication system that implemented a subcarrier multiplexing and wavelength division multiplexing technique based on commercially available light emitting diodes (LEDs). BER reported for 66-cm free-space delivery was 3.8×10^{-3} , but the use of RGB LEDs essentially makes the design out-of-band. To the best of our knowledge, the only in-band design for full-duplex FSOC has been reported by Oh et al., in which communication between a stationary controller and a mobile node is implemented using beam reversibility and data erasure method. Even though this design implements full-duplex operation for the mobile node, the controller has only a transmitter but no receiver. Johnson et al.²⁴ proposed isolating the transmitter and the receiver of a node using a divider, but no functional prototype was demonstrated. In this report, we model the relationship between the divider's suppression capability and the effectiveness of the IBFD link performance and, further, develop an IBFD transceiver prototype that can transfer data over a 3-m link using a single wavelength for both uplink and downlink channels.

2.3 Turbulence Effect on FSO

Light has been a source for communication since the beginning of civilization as lighthouses or signaling beacons, but foggy or rainy weather and atmospheric turbulence limited the extent of the communication. Due to the atmospheric turbulence effect on FSO signals, advancements in optical wireless communication with promising solutions to the turbulence effects has been relatively new. In the last couple of decades, many statistical models have been proposed to characterize the optical wireless channel under turbulent weather. By implementing log—normal or gamma—gamma distribution of the irradiance in an optical channel, performance of the link, such as average channel capacity and signal-to-noise ratio (SNR), has been estimated. However, these works focused on half-duplex configuration of the optical channel. In this work, we carry out weather-dependent performance analysis for an IBFD optical wireless channel.

3 In-Band Full Duplex FSO Transceiver

We developed a prototype of an IBFD-FSO transceiver by utilizing commercially available off-the-shelf hardware and electronic components. The prototype is displayed in Fig. 1. The main parts of the prototype are a Raspberry Pi as the controller and two IrDA2 Clicks,³¹ one of which is used as a transmitter and the other as a receiver. The IrDA2 Clicks are controlled by the Raspberry Pi using two separate threads: T_x thread and R_x thread. We used a Raspberry Pi 3 Model B as the controller, which is a single board computer (Fig. 1). It has a Quad Core 1.2 GHz Broadcom BCM2837 64 bit CPU, 1 GB RAM, BCM43438 wireless local area network (LAN), and 4 USB-2 ports.

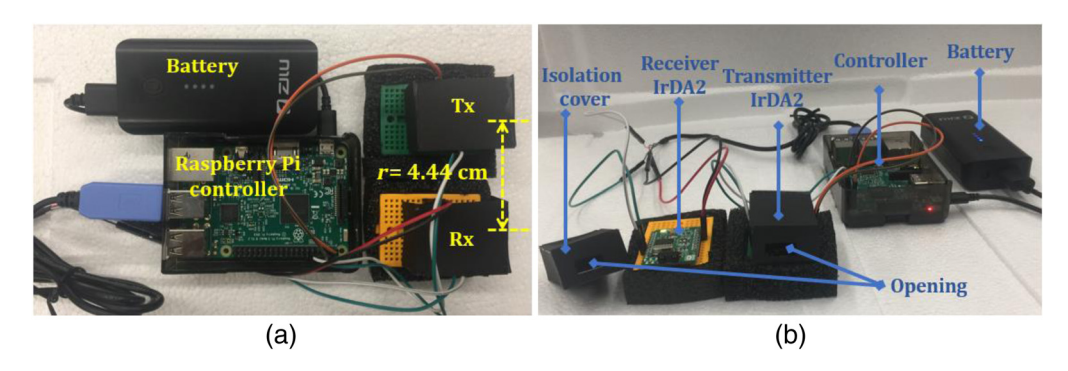


Fig. 1 IBFD-FSO prototype: (a) top view and (b) front view.

3.1 Transceiver

We used two IrDA2 Clicks, 31 one as the transmitter and the other as the receiver. The IrDA2 Click consists of an infrared (IR) transceiver module compliant with the latest IrDA physical layer standard for fast IR data communication. It supports IrDA speeds of up to 115.2 kbit/s. Integrated within the transceiver module are a photo pin diode and infrared emitter (IRED). This device covers the full IrDA range of ≈ 2.75 m using the internal intensity control. The IRED has a peak emission wavelength of 900 nm, and its angle of half intensity is ± 24 deg. The IrDA2 Click board also features the MCP2120, which is a low-cost, high performance, fully static IR encoder/decoder. This device sits between a universal asynchronous receiver–transmitter (UART) and an IR optical transceiver.

3.2 IBFD Operation

The Raspberry Pi has one UART, to which we connected one of the IrDA2 Clicks, which was our transmitter. We used a USB-to-UART converter to connect the other IrDA2 Click to the Pi, which was our receiver. The setup is shown in Fig. 1. Although the IrDA2 Click has both a transmitter and a receiver, it operates only in half-duplex mode. So we used two separate IrDA2s, one of them only for transmission and the other for reception. We prepared two isolating covers, as shown in Fig. 1(b) for the transmitter and the receiver. We used black cardstock papers for building the covers. The cover has only one opening at the front for transmission and reception of signal. All other sides are blocked to prevent optical feedback to the receiver. A schematic block diagram of the transceiver prototype is shown in Fig. 2.

We used Python as the programming language for implementing the IBFD controller at the Raspberry Pi. The main program consists of two separate threads: T_x thread for operating data

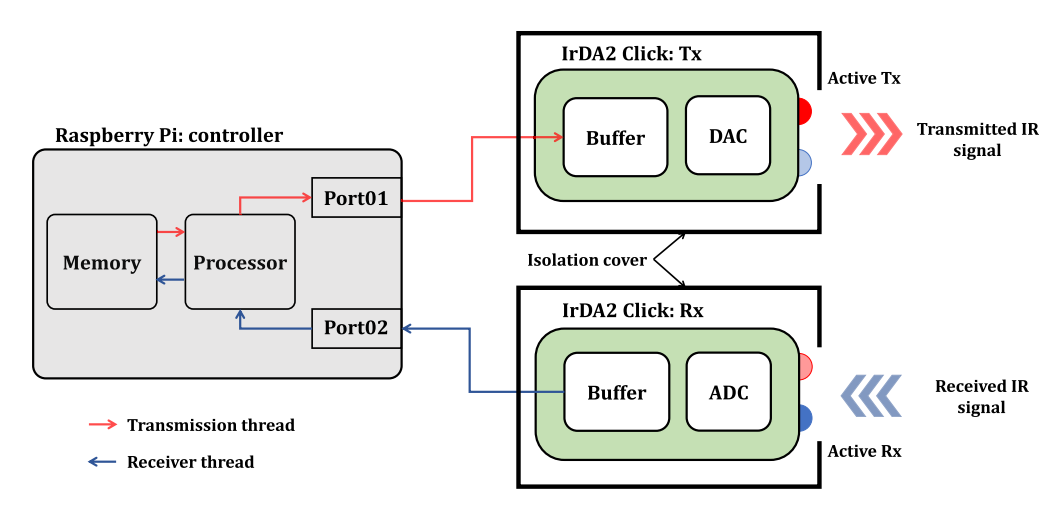


Fig. 2 Block diagram of an IBFD optical transceiver prototype.

Algorithm 1 IBFD-FSO communication threads

```
1: {Initialize the global variables}
2: R<sub>x</sub> = TRUE //Start reception?
3: T_x = TRUE //Start transmission?
{Receives until an empty packet, writes the received data to a file}
1: Local variable r.packet //Buffer of 115.2Kb
2: while R_x = TRUE do
3:
      r.packet ← store received packet
      if r.packet ≠ NULL then
5:
        write r.packet to file
6:
7:
        R_X = FALSE
8:
      end if
   end while
{Reads from a given file until the end and transmits it}
Transmit()
1: Local variable t.packet //Buffer of 115.2 Kb
2: while T_x = TRUE do
3:
      t.packet ← read packet from file
      if t.packet ≠ EOF then
5:
        send t.packet
6:
      else
7:
        T_x = FALSE
      end if
   end while
```

transmission and R_x thread for receiving, processing, and storing the incoming stream of data. The pseudocode of the program is provided in Algorithm 1. The threads do not perform any error control and only read from and write to the receiver and the transmitter, respectively. The transmitter thread reads from a local file and writes chunks of bits (up to 115.2 kb at a time) from the file to the IrDA2 Click transmitter. Likewise, the receiver thread reads from the IrDA2 Click receiver and writes chunks of bits (again, up to 115.2 kb at a time) to a local file. These threads need to be run simultaneously at the Raspberry Pi controller for IBFD operation.

3.3 Experimental Results

We performed real test-bed experiments to gain insight into the effectiveness of the isolator in preventing optical feedback. We used two identical nodes (A and B) with IBFD-FSO transceivers for point-to-point communication. Figure 3(a) shows the image file transmitted between the transceivers during the experiments. The size of this file was 20.1 kbytes. We extracted the RGB pixel intensity values of the image file and created a separate text file of size 755.4 kbytes.

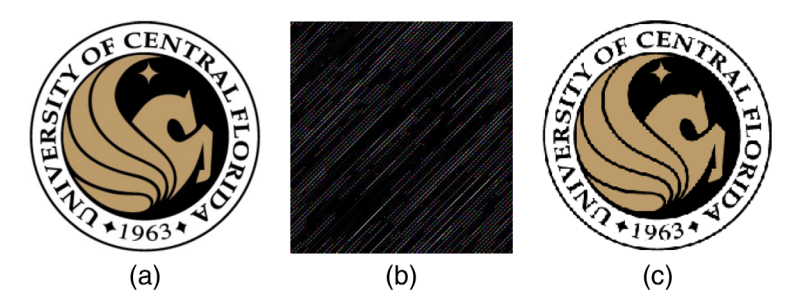


Fig. 3 Transmitted and reconstructed received image, (a) transmitted test image file, (b) received image without isolation, and (c) received image with IBFD-FSO transceiver.

On both nodes A and B, this text file was used for transmission. The Raspberry Pis on both nodes were controlled from a laptop via a secure shell session over Wi-Fi. The laptop and the Pis were all on the same LAN. A simple three-way handshake through the Wi-Fi helped to synchronize the simultaneous operation of the two nodes. After the synchronization, both nodes started listening through their respective IrDA2 receiver. A small delay of (1 s for node A and 2 s for node B) was added before starting the transmission operation on both nodes. This was done to make sure that a node did not start transmitting before the other one was ready to receive data.

First, we performed experiments without using the covers on the transmitters and receivers on both node A and node B. The transmitter and the receiver of a node was kept 4.4 cm apart as shown in Fig. 1(a). The experiment was done on a table with black surface to prevent reflection. The nodes were kept facing each other at a distance of 1 m. The bit error ratios at both nodes were more than 90% because of optical feedback. The received image file is displayed in Fig. 3(b) after reconstruction. We replaced the garbled pixel values with zeros. We conducted the rest of the experiments isolating the transmitter and the receiver of each node as described in Sec. 3.2. A received error-free reconstructed image is shown in Fig. 3(c).

4 Analytical Model of an IBFD-FSO Link

To calculate SINR of an IBFD-FSOC link, we have to consider overall atmospheric attenuation, noise margin, and SI signal. The block diagram of the system, having a link length of *d*, is shown in Fig. 4. The separation distance of the transmitter and the receiver of each transceiver is denoted as *l*. Each node has a controller unit that handles data conversion, queuing, and storage to operate in full-duplex configuration.

When two transceiver nodes communicate with each other in full-duplex configuration, both nodes transmit and receive optical signal simultaneously. Let us consider that x_A and x_B are transmitted signals from nodes A and B, respectively, whereas y_A and y_B represent received signals, respectively. If we denote additive white Gaussian noise as w_A and w_B , then we write the received signals as

$$y_A = \frac{1}{\sqrt{\alpha d^{\gamma}}} \mathcal{H}_{BA} x_B + w_A + i_A(P_A), \tag{1}$$

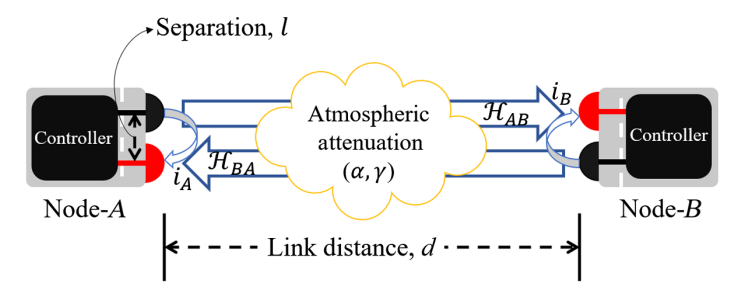


Fig. 4 Block diagram of an IBFD optical wireless link consisting of two nodes.

Table 1 List of symbols.

Symbol	Description
L _{FS}	Free-space loss parameter
T_A	Atmospheric loss parameter
α	Atmospheric attenuation coefficient
γ	Free-space path loss exponent
d	Link distance
1	Separation between transmitter and receiver
V	Visibility
Γ_{s}	Residual SI power
β	Coefficient of SI suppression by separation
μ	Coefficient of SI suppression by isolation
δ	Exponent of SI suppression by isolation
N _T	Average NEP

$$y_B = \frac{1}{\sqrt{\alpha d^{\gamma}}} \mathcal{H}_{AB} x_A + w_B + i_B(P_B), \tag{2}$$

where \mathcal{H}_{AB} and \mathcal{H}_{BA} represent channel impulse functions for the forward and reverse channels, respectively, and $i_A(P_A)$ and $i_B(P_B)$ are the residual SI signals at the nodes. P_A and P_B are the transmitted signal powers at nodes A and B, respectively. Also α is the FSO path loss attenuation coefficient, which we calculated for different visibility conditions in Eq. 7. In Eqs. (1) and (2), d is the distance between two nodes and γ is the free-space path loss exponent of the channel. A typical value of γ for free-space propagation is 2; however, the value can vary for urban areas in the range of 2.7 to 3.5. In this study, we set the value of γ to 2.

A mathematical formulation of the transmission link can be defined by calculating received power by incorporating a weather-dependent atmospheric attenuation coefficient and noise components such as Rayleigh scattering, thermal radiation, and back reflection. A list of important symbols is given in Table 1.

4.1 Atmospheric Attenuation Coefficient

In this section, we will calculate the attenuation of the optical signal over the FSO channel. The optical signal, propagating through free-space medium, experiences different attenuation factors. The received power at the receiver end is given by the Friis transmission equation:³³

$$P_R = P_T G_T G_R T_{\text{atm}} L_{\text{FS}},\tag{3}$$

where P_T is the transmitted power, G_T and G_R are the transmitter and receiver gains, respectively, T_{atm} is the atmospheric transmission coefficient, and L_{FS} is the free-space loss parameter. The free-space loss parameter for an omnidirectional transceiver is given by³³

$$L_{\rm FS} = \left(\frac{\lambda}{4\pi d}\right)^2,\tag{4}$$

where λ is the wavelength of the transmitted signal and d is the link length. For our directional transceiver, we modified the free-space loss parameter using the divergence angle (ϕ) of the transmitter:³⁴

$$L_{\rm FS} = \frac{\lambda^2}{4\pi} \times \frac{A_R}{2\pi d^2 (1 - \cos\phi)},\tag{5}$$

where A_R is the effective receiver area of the detector. The beam footprint (A_{bf}) formed by the source is much larger than the actual receiver area (A_r) . So the effective power received by the receiver is smaller than the power arriving at the receiver plane. Hence, a term is introduced to account for the loss of power which falls outside the receiver area. It is termed as effective receiver area, $A_R = A_r/A_{bf}$.

Attenuation of transmitted power through the atmosphere is dependent on free-space loss and scattering loss, which can be modeled using exponential Beers–Lambert law:³⁵

$$\tau(R) = \frac{P_R}{P_T} = e^{-\alpha d},\tag{6}$$

where α is the attenuation coefficient (per unit length). By equating Eq. (6) to the P_R/P_T ratio from Eq. (3), we calculate the attenuation coefficient as

$$\alpha = \frac{1}{d} \ln \frac{1}{G_T G_R T_{\text{atm}} L_{\text{FS}}}.$$
 (7)

Again, the value of α depends on the wavelength of the signal (λ) , visibility range (V), and size distribution of the particle (q) in the atmosphere. The equation of the atmospheric attenuation coefficient is proposed by Kim et al.³⁶ in the form of

$$\alpha = \frac{3.91}{V} \left(\frac{\lambda}{550 \text{ nm}} \right)^{-q},\tag{8}$$

where q is given by

$$q = \begin{cases} 1.6, & V > 50 \text{ km} \\ 1.3, & 6 \text{ km} < V < 50 \text{ km} . \\ 0.72V^{\frac{1}{3}}, & V < 6 \text{ km} \end{cases}$$
 (9)

By comparing Eqs. (7) and (8), we calculate the gain product G_TG_R . We use this product term to calculate the received power (P_R) for any given transmitted power (P_T) using Eq. (3).

4.2 Atmospheric Turbulence Model

If we consider an FSO system using intensity-modulation/direct detection with on-off keying (OOK), the normalized channel fading coefficient h is considered the product of two random factors, i.e., $h = h_a h_p$, where h_a is the attenuation due to atmospheric turbulence and h_p is the attenuation due to geometric spread.³⁷ The intensity distribution under weak atmospheric turbulence is given by³⁸

$$f_{h_a}(h_a) = \frac{1}{2h_a\sqrt{2\pi\sigma_v^2}} \exp\left[\frac{(\ln h_a + 2\sigma_X^2)^2}{8\sigma_X^2}\right].$$
 (10)

The log-amplitude of the optical intensity has a Gaussian probability density function with variance σ_X^2 given by³⁹

$$\sigma_X^2 = 0.30545k^{7/6}C_n^2z^{11/6} \approx \frac{\sigma_R^2}{4}$$

where C_n^2 is the index of refraction structure parameter (for weak turbulence, $C_n^2 < 1 \times 10^{-14} \text{ m}^{-2/3}$), $k = 2\pi/\lambda$ is the optical wavenumber, z is the propagation distance, and σ_R^2 is the Rytov variance defined as

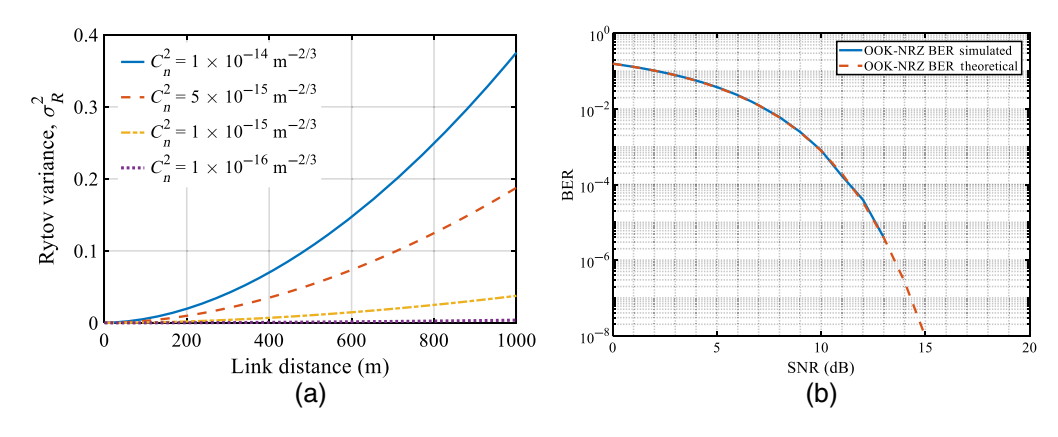


Fig. 5 Atmospheric turbulence model for FSO link utilizing OOK modulation scheme, (a) Rytov variance over link distance and (b) BER vs SNR plot for turbulent channel.

$$\sigma_R^2 = 1.23k^{7/6}C_n^2z^{11/6}$$
.

In the presence of weak atmospheric turbulence, the SNR is expressed as 40,41

$$SNR = (0.30545k^{7/6}C_n^2z^{11/6})^{-1}. (11)$$

For the FSO link with the OOK modulation scheme, the BER is, then, expressed as 42

$$BER = \frac{\exp(-SNR/2)}{(2\pi SNR)^{0.5}}.$$
 (12)

Figure 5(a) shows the Rytov variance for plane waves of $\lambda = 900$ nm calculated at different turbulence levels over a range of propagation distance. BER versus SNR curve for the turbulent channel using the OOK modulation scheme is shown in Fig. 5(b). To achieve BER below 10^{-8} , the SNR of the system SNR needs to be >15 dB.

4.3 Noise Calculation

The variance in the current noise when an optical signal is received by the detector is given by

$$\sigma_N^2 = \sigma_{\text{th}}^2 + \sigma_R^2 + \sigma_{\text{dark}}^2 + \sigma_T^2, \tag{13}$$

where σ_{th}^2 , σ_B^2 , σ_{dark}^2 , and σ_T^2 are the noise variance in the current due to Johnson (thermal) noise, background radiation, dark current, and transmitted signal, respectively. Noise equivalent power (NEP) is defined as the quantitative measure of the sensitivity of a detector or the power generated by a source of noise on a detector. The equations for the NEP of the optical components are given by σ_T^{47}

$$P_{\text{bg_sn}} = \frac{\sqrt{2qSP_{\text{bg}}B_{\text{en}}F}}{S},\tag{14}$$

$$P_{\text{sig_sn}} = \frac{\sqrt{2qSP_{\text{sig}}B_{\text{en}}F}}{S},\tag{15}$$

$$P_{\text{dark_sn}} = \frac{\sqrt{(2qI_{\text{dark}}G_{\text{det}}^2F + 2qI_{\text{dc}})B_{\text{en}}}}{SG_{\text{det}}},$$
(16)

where $P_{\rm bg}$ is the optical solar background noise, $P_{\rm sig}$ is the optical power of the signal, $I_{\rm dark}$ is the optical dark current, $I_{\rm dc}$ is the dc dark current, $G_{\rm det}$ is the detector current gain, $B_{\rm en}$ is the effective noise bandwidth $(=\frac{\pi B}{2})$, S is the radiant sensitivity of the detector (amp/watt), F is the excess noise factor which is equal to 1 for photodiode, and q is the electronic charge. The total NEP is given by

$$N_T = \sqrt{P_{\text{bg_sn}}^2 + P_{\text{sig_sn}}^2 + P_{\text{dark_sn}}^2}.$$
 (17)

To design a short-range FSOC system using a laser as the transmitter, all of the noise contributions need to be incorporated into the calculation. As the bit-rate requirement is increasing day-by-day, receiver components and circuit are required to be very sensitive and responsive. With the increase of sensitivity, the receiver noise budget becomes smaller.

4.4 Residual Self-Interference Model

Using the residual SI model of Refs. 6 and 48, residual SI powers at nodes A and B are given by

$$\Gamma_{sA} = \frac{P_A^{1-\delta}}{\beta \mu^{\delta}} \quad \text{and} \quad \Gamma_{sB} = \frac{P_B^{1-\delta}}{\beta \mu^{\delta}},$$
(18)

where β represents the coefficient of SIC by separation of the transmitter and the receiver within the same transceiver unit and μ and δ represent SI suppression parameters for the deployed passive SI cancellation technique. P_A and P_B are the transmitted signal powers at nodes A and B, respectively.

Within a transceiver unit, the distance between the transmitter and receiver is denoted as l and the coefficient of the passive SIC coefficient is μ . The exponent of passive SIC is denoted as δ , which can be any value from 0 to ∞ . The case $\delta=0$ represents when no passive SIC is implemented, whereas $\delta=\infty$ represents perfect cancellation of SI. Again, $\delta=1$ means there is a constant residual SI power present irrespective of the transmit power, which portrays an unrealistic scenario for full-duplex application. However, there is threshold value of δ for which full-duplex performance supercedes the performance of half-duplex operation, which can be defined as δ^* . The typical value for δ^* lies between 0.6 to 0.8. Usually, it can be defined that any value of δ that is less than δ^* represents low SIC and a higher δ value represents high SIC. For this study, we will consider $\delta=0.2$ for low SIC and $\delta=1.8$ for high SIC performance.

The value of the coefficient of SIC by separation β depends on the distance (l) of the transmitter and receiver within a transceiver unit and the free space attenuation coefficient. The equation is defined as

$$\beta = \alpha_{\perp} l^{\gamma}, \tag{19}$$

where α_{\perp} is the free space attenuation coefficient along the perpendicular direction of beam propagation and γ is the free space path loss exponent. Considering $l \ll d$ and a comparatively higher divergence angle (θ) of the VCSEL, the value of α_{\perp} will be comparable to the value of the free-space attenuation coefficient (α) for our system. For this study, we will consider $\alpha_{\perp} \approx \alpha$ and $\gamma = 2$.

4.5 SINR Calculation

In the previous sections, we have shown the formulation of free-space atmospheric attenuation, noise components, and residual SI. Let us consider a system consisting of two transceiver nodes, each having one transmitter and one receiver. Using these equations, SINR can be written for a transceiver with the transmitter having a θ divergence angle and the receiver with a detection area of $A_{\rm det}$ as

$$SINR_A = \frac{P_B T_{atm}(V) \lambda^2 A_{det}}{8\pi^2 d^2 (1 - \cos\theta) (N_{TA} + \Gamma_{sA})},$$
(20)

$$SINR_B = \frac{P_A T_{atm}(V) \lambda^2 A_{det}}{8\pi^2 d^2 (1 - \cos\theta) (N_{TB} + \Gamma_{cB})},$$
(21)

where N_{TA} and N_{TB} denote NEP at node A and B, respectively.

5 Simulation Results and Discussion

In this section, we will present our simulation results for the performance of an IBFD transceiver for different weather conditions and SI suppression parameters. The transceiver model is developed using a VCSEL as the transmitter and Si PIN photodiode as the receiver. VCSELs are semiconductor laser diodes that can emit a coherent light beam normal to the substrate surface. In most cases, the active region consists of several quantum wells and is electrically pumped via circular ring electrodes. 49 This specific design of lasers is advantageous in many areas compared with edge-emitting lasers or LEDs, such as low threshold current, circular mode profile, high-speed modulation for communication, and most importantly, two-dimensional arraying capability for multielement optical component design.⁵⁰ Due to the short-resonator round-trip time, VCSELs can be modulated with frequencies well in the gigahertz range, which makes them useful as transmitters for FSO communications. The most common emission wavelengths of commercially available VCSELs are in the range of 850 to 980 nm, as obtained with the GaAs/AlGaAs material system. However, longer wavelengths of 1.3, 1.55, or even beyond $2 \mu m$ (as required for gas sensing) can be obtained with dilute nitrides (GaInNAs quantum wells on GaAs). For short-range communications, 850-nm VCSELs are used in combination with multimode fibers and for a large aperture area the bitrate can be as high as 25 Gbit/s.⁵¹

The output beam from VCSEL operation can be either continuous-wave (CW) or pulsed, depending on the design and vertical thermal distribution of the active region through the distributed Bragg reflectors. Several research groups have already demonstrated CW operation at room temperature for VCSELs.^{52–54} All of these reasons make VCSEL operating at a 850 to 900 nm wavelength a better candidate as a transmitter for FSO communication and sensing application compared with other light sources.^{55,56}

The system parameters used for the simulation are listed in Table 2.

5.1 Attenuation Coefficient and Link Length

To calculate the atmospheric attenuation coefficient of the FSO signal, we implemented Eq. (6) using parameters of the system components at $\lambda=900\,$ nm. We used detector parameters such as receiver area ($A_R=1\,$ cm²) and transmitter parameters such as divergence angle ($\theta=24\,$ deg) to calculate free-space loss parameter $L_{\rm FS}$. We acquired atmospheric loss coefficient $T_{\rm atm}$ from MODTRAN® simulation for different visibility ranges. MODTRAN® simulation parameters are listed in Table 3. We calculated atmospheric attenuation coefficient α using Eqs. (3)–(6). The calculated α and corresponding link distance L are shown in Fig. 6. It can be seen from this figure that the link distance is about 127 m when visibility is 1 km. With the increase of visibility, the link distance also increases, as we observe from this figure; however, it tends to plateau at around 132 m.

The attenuation coefficient due to FSO loss is highly dependent on the visibility of the atmosphere. Using the model described by Kim et al.,³⁶ we can estimate the attenuation coefficient and corresponding permissible link distance. It can be noted from Eq. (8) that the path loss exponent

ParameterValue (unit)Wavelength (λ)900 nmBandwidth (BW)175 MHzTransmit power (P_T)10 mWDivergence angle (θ)24 degField of view120 degReceiver area (A_r)1 cm²

Table 2 System parameters for simulation.

Table 3 MODTRAN simulation parameters.

Item	Value/description	Unit
Atmospheric model	Mid-latitude winter model	
Water	1059.7	atm cm
Ozone	0.37681	atm cm
CO ₂	410	ppmv
CO	0.15	ppmv
CH ₄	1.8	ppmv
Temperature	300	K
Aerosol model	Urban	

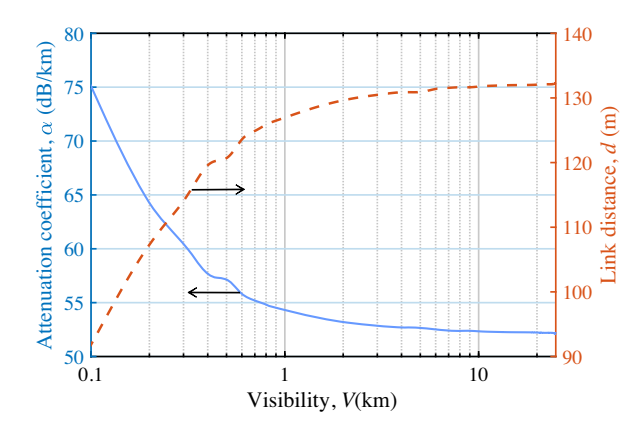


Fig. 6 Attenuation coefficient and link distance variation with visibility using system parameters.

depends on visibility only; as a result the model over-estimates the link distance for higher visibility regions. However, from the fitting model described in Eq. (8), we can estimate that compared with a 1550 nm wavelength, signal at 900 nm experiences a smaller attenuation coefficient and, hence, attains a higher link distance. We also calculated the attenuation coefficient for different wavelengths. As we observe from Fig. 7, smaller wavelength and higher visibility lead to a smaller attenuation coefficient.

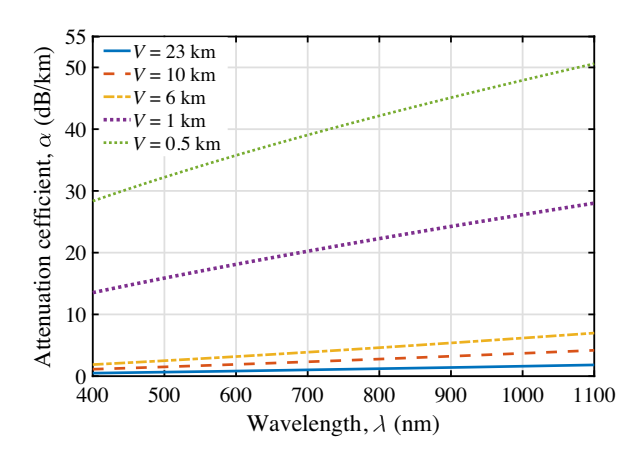


Fig. 7 Attenuation coefficient variation with wavelength.

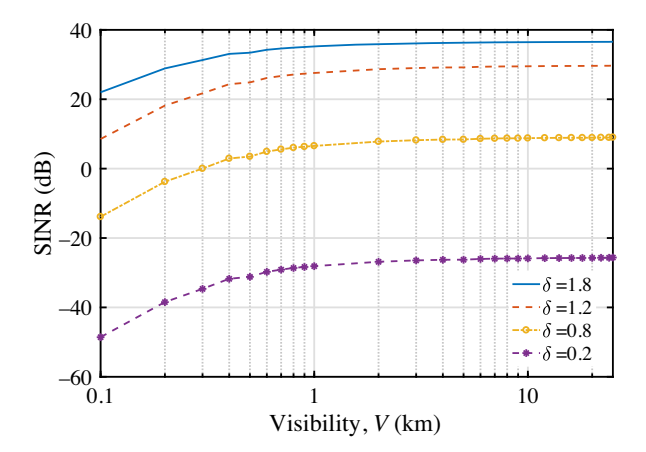


Fig. 8 SINR variation for different visibility ranges.

5.2 Behavior of SINR

To evaluate SINR in the FSO channel, we considered two nodes, A and B, and established communication in a full-duplex manner. For this set of simulations, we set one transmitter and one receiver in each transceiver module, separated by a distance of l=5 cm. We presented the model for SINR_A and SINR_B in Eqs. (20) and (21), respectively. We calculated SI suppression by the separation coefficient β using Eq. (19). The value of β depends on the separation distance (l) and positions of the transmitter and the receiver in the same transceiver unit, whereas the value of the SI suppression by the passive isolation coefficient μ represents the level of SI reduction when the passive SI suppression technique is implemented. We set $\mu=10$ dB to a constant value for our simulations. SI suppression by the isolation exponent δ is varied to determine residual SI power at the receiver. The average NEP power N_T is calculated based on the formulation presented in the previous section.

The level of SI suppression is calculated while we set δ for different visibility ranges. As shown in Fig. 8, SINR for a node changes depending on the δ value. The SINR value is calculated using Eq. (20) for different δ values. We can see from this figure that as the SIC level gets stronger (larger δ), the performance of the channel gets better. Again, the value of SINR is strongly dependent on the atmospheric attenuation. Hence with the increase of visibility and by comparing the value of the attenuation level from Fig. 6, we clearly see improvement in channel performance as the visibility range (V) increases.

Figure 9(a) shows the SINR behavior for different δ under different transmit power levels. As δ increases and the level of SIC improves, SINR performance gets better. For smaller δ values, SIC suppression is weak and SINR is mostly dominated by NEP present in the system.

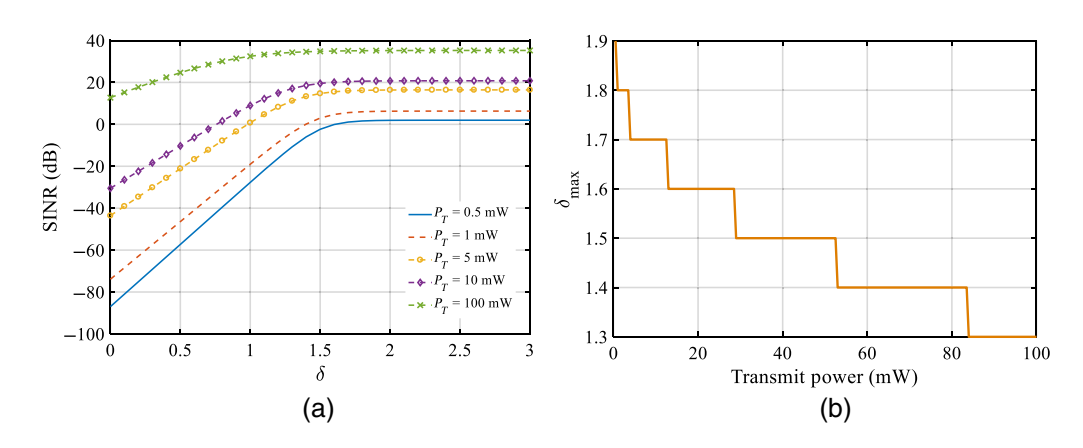


Fig. 9 (a) SINR variation at different transmit power levels with the change of δ . (b) SINR variation at node B for different visibility conditions and transmit power levels.

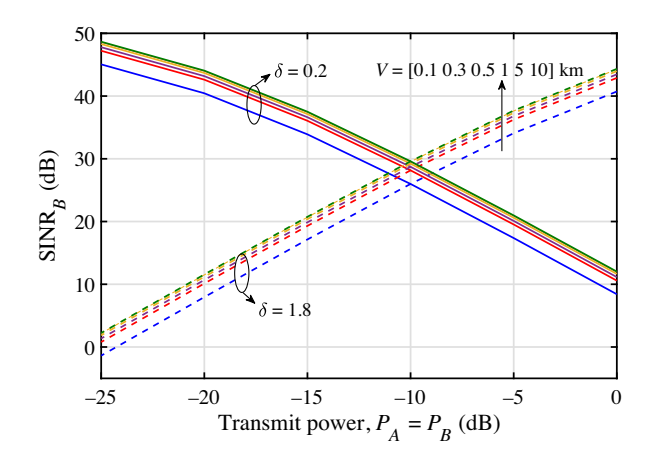


Fig. 10 SINR variation at node B for different visibility conditions and transmit power levels.

We can see from Fig. 9(a) that SINR becomes constant after a level of SI suppression because residual SI signal becomes too weak compared with AWGN signal present in the channel that any further improvement in active SI suppression does not improve the performance of the transceiver. We also calculated δ_{max} , which can be defined as the maximum value of δ for which the SINR of the link gets saturated for different transmit power levels. We observe the declining trend of required δ_{max} with the increase of the transmit power in Fig. 9(b). The optimum value of the exponent δ can be calculated from the model presented in this work.

Figure 10 indicates that, when both nodes are transmitting at the same power level, SINR improves with the increase of visibility. As the value of β depends on the transmit power, β needs to be recalculated for each transmit power level. We also show SINR variation for $\delta = 0.2$ and $\delta = 1.8$, with both nodes transmitting same power, in Fig. 10. For the weak SI suppression ($\delta = 0.2$) case, SINR decreases with increase of transmission power because, with weak SI suppression, residual SI signal increases with the increase of the transmit power. By contrast, for strong SI suppression ($\delta = 1.8$), SINR improves with higher transmission power.

Shannon's theorem gives an upper bound to the capacity of a link, in bits per second (bps), as a function of the available bandwidth and the SINR of the link. In our case, the maximum data rate that can be achieved theoretically depends on the SINR of the FSO link. We have seen from Fig. 5(b) that, to achieve an acceptable communication link, the SINR value should be >15 dB. We have also observed from Figs. 8, 9(a), and 10 that SINR attained from our proposed laser-based IBFD-FSO system can be up to 40 dB. We calculated the maximum data capacity for this SINR range (15 to 40 dB) using Shannon's theorem. From Fig. 11, we observe that the maximum capacity varies from 800 Mbps up to 2.3 Gbps if the SINR of the system changes from 15 to 40 dB for a system bandwidth of 175 MHz. As the transmit power is growing exponentially,

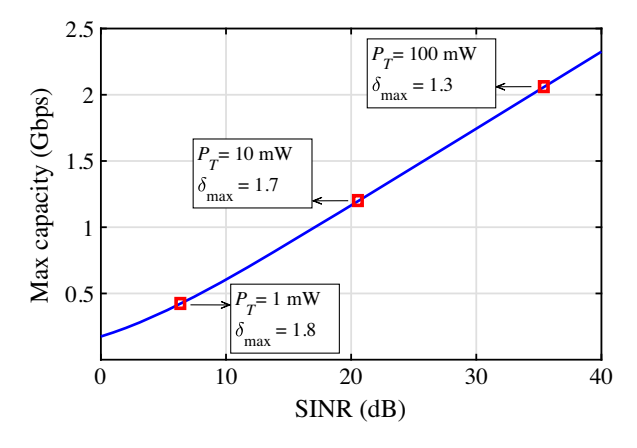


Fig. 11 Shannon's limit for maximum capacity of the IBFD-FSO link.

the maximum capacity is growing roughly linearly as expected by Shannon's theorem. But, an interesting insight is that, as the transmit power increases, the maximum passive isolation efficiency exponent (δ_{max}) needed to attain the maximum capacity reduces roughly linearly. This trade-off between the transmit power and δ_{max} (which typically corresponds to the thickness of the isolation material) can be exploited when maximizing attainable link capacity while conforming to certain size, weight, and power requirements of the mobile platform.

6 Conclusion

We modeled the effect of atmospheric attenuation and corresponding link length for an IBFD optical transceiver design in various cases. We considered the effects of passive and active SI suppression and how the performance of the optical channel can be improved or made immune to SI by taking into account the design parameters, such as transmit power and receiver positioning. We proposed a mathematical model for passive SIC by the isolation technique. We calculated background noise and residual SI power to measure the performance of the channel by calculating SINR of the communication link. We observed that, even with high visibility ($V \ge 1$ km), link length of the FSO channel is limited to ≈ 120 m when the distance between the transmitter and the receiver of the full-duplex transceiver is 5 cm. We also presented the performance of the channel based on the SI suppression level (δ).

Some future works may include experimental implementation of the ideas presented in this paper. In our prior work, we have demonstrated a prototype of an IBFD transceiver. Some design improvements and further advancements that address SI and atmospheric effect on the performance of the transceiver are in progress. We presented the formulation of the SI suppression model to evaluate the performance under IBFD operation. Again, sidelobe modeling of a VCSEL is also an open problem that needs to be addressed. Even though FSO can achieve very high bit rate, range limitation due to high attenuation and weather dependency has always been a hard challenge to overcome. Potential futuristic wireless communication for mobile and secure *ad hoc* FSO networks will require implementation of IBFD-FSO transceivers that increase the network capacity to improve the performance and reliability of the link.

Acknowledgments

This work was supported in part by the US National Science Foundation Award No. 1836741.

References

- A. Sevincer, M. Bilgi, and M. Yuksel, "Automatic realignment with electronic steering of free-space-optical transceivers in MANETs: a proof-of-concept prototype," *Ad Hoc Networks* 11, 585–595 (2013).
- M. Khan, M. Yuksel, and G. Winkelmaier, "GPS-free maintenance of a free-space-optical link between two autonomous mobiles," *IEEE Trans. Mob. Comput.* 16(6), 1644–1657 (2017).
- 3. M. Khan and M. Yuksel, "Autonomous alignment of free-space-optical links between UAVs," in *Proc. 2nd Int. Workshop Hot Top. in Wireless*, ACM, pp. 36–40 (2015).
- 4. C. W. J. Oh et al., "10 Gbps all-optical full-duplex indoor optical wireless communication with wavelength reuse," in *OFC*, Optical Society of America, p. Th4A-6 (2016).
- 5. X. Xie and X. Zhang, "Does full-duplex double the capacity of wireless networks?" in *INFOCOM*, IEEE (2014).
- 6. K. Akcapinar and O. Gurbuz, "Full-duplex bidirectional communication under self-interference," in *13th Int. Conf. Telecommun. (ConTEL)*, IEEE, pp. 1–7 (2015).
- 7. S. Goyal et al., "A distributed MAC protocol for full duplex radio," in *Asilomar Conf. Signals, Syst. Comput.*, IEEE, pp. 788–792 (2013).
- 8. Z. Zhang and B. Li, "Neighbor discovery in mobile ad hoc self-configuring networks with directional antennas: algorithms and comparisons," *IEEE Trans. Wireless Commun.* **7**(5), 1540–1549 (2008).

- E. Everett et al., "Empowering full-duplex wireless communication by exploiting directional diversity," in *Signals, Syst. Comput. (ASILOMAR), Conf. Rec. Forty Fifth Asilomar Conf.*, IEEE, pp. 2002–2006 (2011).
- E. Everett, A. Sahai, and A. Sabharwal, "Passive self-interference suppression for full-duplex infrastructure nodes," *IEEE Trans. Wireless Commun.* 13(2), 680–694 (2014).
- 11. E. J. Mayeux, "Optical transceiver for free-space communication links," U.S. Patent No. 5,390,040 (1995).
- 12. K. Wang et al., "Experimental demonstration of full-duplex optical wireless personal area communication system with 16-CAP modulation," in *Opt. Fiber Commun. Conf. and Exhibit. (OFC)*, IEEE, pp. 1–3 (2015).
- 13. K. Wang et al., "Full-duplex gigabit indoor optical wireless communication system with CAP modulation," *IEEE Photonics Technol. Lett.* **28**(7), 790–793 (2016).
- 14. P. Zhang et al., "Link budget and simulation of double-wavelength full-duplex free-space laser communication based on modulating retro-reflector," in *Wireless Communications*, *Networking and Applications*, Q. A. Zeng, Ed., Lecture Notes in Electrical Engineering, Vol. 348, pp. 285–293, Springer, New Delhi (2016).
- 15. A. S. Haq, M. R. Khan, and M. Yuksel, "A prototype of in-band full-duplex free-space optical transceiver," in *IEEE Int. Symp. Local and Metropolitan Area Networks (LANMAN)*, IEEE, pp. 112–113 (2018).
- A. S. Haq and M. Yuksel, "Weather limited short-range in-band full-duplex free-space optical transceiver," *Proc. SPIE* 10910, 1091021 (2019).
- 17. A. Sabharwal et al., "In-band full-duplex wireless: challenges and opportunities," *IEEE J. Sel. Areas Commun.* **32**(9), 1637–1652 (2014).
- 18. D. Kim, H. Lee, and D. Hong, "A survey of in-band full-duplex transmission: from the perspective of PHY and MAC layers," *IEEE Commun. Surv. Tutorials* **17**(4), 2017–2046 (2015).
- 19. J. I. Choi et al., "Achieving single channel, full duplex wireless communication," in *Proc. Sixteenth Annu. Int. Conf. Mob. Comput. and Networking*, ACM, pp. 1–12 (2010).
- 20. D. Kim et al., "Transmission capacity of full-duplex-based two-way ad hoc networks with ARQ protocol," *IEEE Trans. Veh. Technol.* **63**(7), 3167–3183 (2014).
- 21. M. Jain et al., "Practical, real-time, full duplex wireless," in *Proc. 17th Annu. Int. Conf. Mob. Comput. and Networking*, ACM, pp. 301–312 (2011).
- 22. M. Duarte et al., "Design and characterization of a full-duplex multiantenna system for WiFi networks," *IEEE Trans. Veh. Technol.* **63**(3), 1160–1177 (2014).
- 23. Y. Wang et al., "Demonstration of 575-Mb/s downlink and 225-Mb/s uplink bi-directional SCM-WDM visible light communication using RGB LED and phosphor-based LED," *Opt. express* **21**(1), 1203–1208 (2013).
- 24. B. E. Johnson et al., "Wide-angle, high-speed, free-space optical communications system," U.S. Patent No. 5,359,446 (1994).
- 25. A. K. Majumdar, "Free-space laser communication performance in the atmospheric channel," *J. Opt. Fiber Commun. Rep.* **2**(4), 345–396 (2005).
- A. Al-Habash, L. C. Andrews, and R. L. Phillips, "Mathematical model for the irradiance probability density function of a laser beam propagating through turbulent media," *Opt. Eng.* 40(8), 1554–1563 (2001).
- F. S. Vetelino, C. Young, and L. Andrews, "Fade statistics and aperture averaging for Gaussian beam waves in moderate-to-strong turbulence," *Appl. Opt.* 46(18), 3780–3789 (2007).
- S. S. Muhammad, P. Kohldorfer, and E. Leitgeb, "Channel modeling for terrestrial free space optical links," in *Proc.* 2005 7th Int. Conf. Transparent Opt. Networks, IEEE, vol. 1, pp. 407–410 (2005).
- 29. H. E. Nistazakis et al., "Average capacity of optical wireless communication systems over atmospheric turbulence channels," *J. Lightwave Technol.* **27**(8), 974–979 (2009).
- K. P. Peppas et al., "Average capacity of optical wireless communication systems over IK atmospheric turbulence channels," *IEEE/OSA J. Opt. Commun. Networking* 4(12), 1026–1032 (2012).
- 31. "IrDA2 Click," http://www.mikroe.com/click/irda2/.

- 32. V. Abhayawardhana et al., "Comparison of empirical propagation path loss models for fixed wireless access systems," in *IEEE 61st Veh. Technol. Conf., VTC 2005-Spring*, IEEE, vol. 1, pp. 73–77 (2005).
- 33. H. Manor and S. Arnon, "Performance of an optical wireless communication system as a function of wavelength," *Appl. Opt.* **42**(21), 4285–4294 (2003).
- 34. D. C. O'Brien et al., "Short-range optical wireless communications," in *Wireless World Research Forum*, pp. 1–22 (2005).
- 35. H. Weichel, *Laser Beam Propagation in the Atmosphere*, vol. 3, SPIE Press, Bellingham, Washington (1990).
- 36. I. I. Kim, B. McArthur, and E. J. Korevaar, "Comparison of laser beam propagation at 785 nm and 1550 nm in fog and haze for optical wireless communications," *Proc. SPIE* **4214**, 26–38 (2001).
- 37. H. G. Sandalidis et al., "BER performance of FSO links over strong atmospheric turbulence channels with pointing errors," *IEEE Commun. Lett.* **12**(1), 44–46 (2008).
- 38. H. Kaushal, V. K. Jain, and S. Kar, *Free Space Optical Communication*, Vol. 1, Springer, Gurgaon, Haryana (2017).
- 39. I. Alimi et al., "Challenges and opportunities of optical wireless communication technologies," in *Optical Communication Technology*, IntechOpen, Pedro Pinho (2017).
- 40. M. A. A. Ali and A. Ali, "Atmospheric turbulence effect on free space optical communications," *Int. J. Emerging Technol. Comput. Appl. Sci.* **5**(4), 345–351 (2013).
- 41. A. C. Motlagh et al., "The effect of atmospheric turbulence on the performance of the free space optical communications," in *6th Int. Symp. Commun. Syst.*, *Networks and Digital Signal Process.*, IEEE, pp. 540–543 (2008).
- 42. G. Xu et al., "Influence of atmospheric turbulence on FSO link performance," *Proc. SPIE* **5281**, 816–823 (2004).
- 43. S. G. Lambert and W. L. Casey, Laser Communications in Space, Artech House (1995).
- 44. N. S. Kopeika, *A System Engineering Approach to Imaging*, SPIE Press, Bellingham, Washington (1998).
- 45. A. Yariv, *Optical Electronics*, Saunders College Publishing (1991).
- 46. S. Leclercq, "Discussion about noise equivalent power and its use for photon-noise calculation," in *Rep. on FOV Opt. and Bolometer Projects for the 30 m Telesc.*, International Research Institute for Radio Astronomy (IRAM), pp. 1–15 (2007).
- 47. J. W. Giles and I. N. Bankman, "Underwater optical communications systems. Part 2: Basic design considerations," in *MILCOM* 2005-2005 IEEE Mil. Commun. Conf., IEEE, pp. 1700–1705 (2005).
- 48. M. Duarte, C. Dick, and A. Sabharwal, "Experiment-driven characterization of full-duplex wireless systems," *IEEE Trans. Wireless Commun.* **11**(12), 4296–4307 (2012).
- 49. Y.-S. Liu et al., "Optically pumped vertical-cavity surface-emitting laser at 374.9 nm with an electrically conducting n-type distributed Bragg reflector," *Appl. Phys. Express* **9**(11), 111002 (2016).
- 50. R. Michalzik, VCSELs: Fundamentals, Technology And Applications Of Vertical-Cavity Surface-Emitting Lasers, vol. 166, Springer (2012).
- 51. P. Westbergh et al., "Large aperture 850 nm vcsels operating at bit rates up to 25 gbit/s," *Electron. Lett.* **44**(15), 907–908 (2008).
- 52. T.-C. Lu et al., "CW lasing of current injection blue GAN-based vertical cavity surface emitting laser," *Appl. Phys. Lett.* **92**(14), 141102 (2008).
- 53. Y. Higuchi et al., "Room-temperature CW lasing of a GAN-based vertical-cavity surface-emitting laser by current injection," *Appl. Phys. Express* **1**(12), 121102 (2008).
- 54. C. A. Forman et al., "Continuous-wave operation of m-plane GAN-based vertical-cavity surface-emitting lasers with a tunnel junction intracavity contact," *Appl. Phys. Lett.* **112**(11), 111106 (2018).
- 55. A. Liu et al., "Vertical-cavity surface-emitting lasers for data communication and sensing," *Photonics Res.* **7**(2), 121–136 (2019).
- 56. I. S. Amiri et al., "Spatial continuous wave laser and spatiotemporal VCSEL for high-speed long haul optical wireless communication channels," *J. Opt. Commun.* 1, ahead-of-print (2019).

Abul F. M. S. Haq received his BSc and MSc degrees in EEE from Bangladesh University of Engineering and Technology (BUET), Bangladesh, in 2012 and 2014, respectively, and his MSc degree in electrical and computer engineering from Georgia Institute of Technology in 2015. He is a PhD candidate in the Department of Optics and Photonics at CREOL of the University of Central Florida (UCF). His research interests include integrated system design, sensor design, wireless connectivity, optical wireless communication, free-space-optics, opto-electronics devices, and fabrication techniques. He is a student member of SPIE, SPIE, and OSA.

Murat Yuksel received his BS degree in computer engineering from Ege University, Izmir, Turkey, in 1996, and his MS degree and PhD in computer science from Rensselaer Polytechnic Institute (RPI), Troy, New York, USA, in 1999 and 2002, respectively. He is an associate professor in the ECE Department, UCF, Orlando, Florida, USA. His research interests are in the area of networked, wireless, and computer systems with a recent focus on big-data networking, UAV networks, optical wireless, public safety communications, device-to-device protocols, economics of cyber-security and cyber-sharing, routing economics, network management, and network architectures. He has been on the editorial board of *Computer Networks* and published more than 150 papers at peer-reviewed journals and conferences. He is a co-recipient of the IEEE LANMAN 2008 Best Paper Award. He is a senior member of IEEE and a senior and life member of ACM and was a member of Sigma Xi and ASEE.